# Periodic Orbits and Disturbance Growth for Baroclinic Waves

R. M. SAMELSON

*College of Oceanic and Atmospheric Sciences, Oregon State University, Corvallis, Oregon*

(Manuscript received 3 January 2000, in final form 23 June 2000)

ABSTRACT

The growth of linear disturbances to stable and unstable time-periodic basic states is analyzed in an asymptotic model of weakly nonlinear, baroclinic wave–mean interaction. In this model, an ordinary differential equation for the wave amplitude is coupled to a partial differential equation for the zonal-flow correction. Floquet vectors, the eigenmodes for linear disturbances to the oscillatory basic states, split into wave-dynamical and decaying zonal-flow modes. Singular vectors reflect the structure of the Floquet vectors: the most rapid amplification and decay are associated with the wave-dynamical Floquet vectors, while the intermediate singular vectors closely follow the decaying zonal-flow Floquet vectors. Singular values depend strongly on initial and optimization times. For initial times near wave amplitude maxima, the Floquet decomposition of the leading singular vector depends relatively weakly on optimization time. For the unstable oscillatory basic state in the chaotic regime, the leading Floquet vector is tangent to the large-scale structure of the attractor, while the leading singular vector is not. However, corresponding inferences about the accessibility of disturbed states rely on the simple attractor geometry, and may not easily generalize. The primary mechanism of disturbance growth on the wave timescale in this model involves a time-dependent phase shift along the basic wave cycle. The Floquet vectors illustrate that modal disturbances to time-dependent basic states can have time-dependent spatial structure, and that the latter need not indicate nonmodal dynamics. The dynamical splitting reduces the ''butterfly effect,'' the ability of small-scale disturbances to influence the evolution of an unstable large-scale flow.

## 1. Introduction

Although it is natural to presume that the atmosphere has a unique past, present, and future, a given model of the atmosphere may have many histories, corresponding either to different initial conditions or to different definitions of the zero of time. In numerical weather prediction, ensemble forecasting has been developed to exploit this freedom, by combining multiple model predictions in an attempt to improve a single atmospheric forecast (Epstein 1969; Leith 1974).

Two different techniques for ensemble generation have recently been implemented in operational global numerical weather prediction models: bred growing modes (Toth and Kalnay 1997) and singular vectors (Buizza et al. 1993; Ehrendorfer and Tribbia 1997). Bred growing modes are computed by a repeated ''breeding'' cycle, in which the differences between forecast ensemble members and a control forecast is rescaled and added to the analysis at each analysis cycle to initialize a new ensemble. Singular vectors are optimal disturbances (Lorenz 1965; Farrell 1989) computed by maximizing specific measures of disturbance growth over predetermined forecast intervals.

The spread and distribution of a forecast ensemble provide predictive information that is not available from individual model forecasts. The behavior of forecast ensembles, of course, also reflects the physics of the atmosphere, as represented by the corresponding models. One might hope that the study of the physics of these ensembles might lead to insights into the dynamics of the atmosphere, as well as to improved forecasting techniques. A number of studies have begun to address questions regarding the physical and dynamical content of singular vectors and bred growing modes in systems ranging in complexity from the low-order Lorenz (1963) equations to operational numerical weather prediction models (e.g., Buizza and Palmer 1995; Buizza 1995; Trevisan and Legnani 1995; Legras and Vautard 1996; Szunyogh et al. 1997; Vannitsem and Nicolis 1997).

The present contribution is an effort in this latter direction. The object is to compute and analyze singular vectors and the simplest analogs of bred growing modes in a model of baroclinic wave–mean interaction that is physically consistent but still simple enough to admit a fairly complete analysis, at least for specific parameter values. The overall goal is to improve insight into the processes of disturbance growth in time-dependent baroclinic flows. The dynamics studied here are the as-

*Corresponding author address:* Dr. R. M. Samelson, College of Oceanic and Atmospheric Sciences, 104 Ocean Admin. Bldg., Oregon State University, Corvallis, OR 97331-5503.
E-mail: rsamelson@oce.orst.edu

ymptotic wave–mean interaction equations derived by Pedlosky (1971) and studied further by Pedlosky and Frenzen (1980) and Klein and Pedlosky (1986). These equations describe the evolution of a weakly nonlinear baroclinic wave and a zonal flow correction for a zonal flow near marginal stability. This is the simplest physical model of nonlinear baroclinic dynamics that is currently available. It represents the extension to weak nonlinearity of the Phillips (1954) two-layer model of linear baroclinic instability, and is summarized in a popular pedagogical text (Pedlosky 1987). It retains much of the simplicity of the Lorenz (1963) equations, to which it is related (Pedlosky and Frenzen 1980). By virtue of its asymptotic derivation, it also admits a direct geophysical interpretation in the parameter regime of most interest.

The analysis focuses on disturbances to periodic solutions of these model equations. Periodic solutions offer a convenient framework for investigating the behavior of linear disturbances to time-dependent basic states, which is intermediate between the study of disturbances to steady flows (e.g., Phillips 1954) and the study of disturbances to flows with general time dependence (e.g., Joly and Thorpe 1991; Farrell and Ioannou 1996). Since the cycles are time-dependent, they present many of the same obstacles to analysis as more general flows. But, since each cycle has a definite period, and a distinct and well-defined spatiotemporal structure that is determined by the evolution of the system over a finite time, they have intuitively appealing identities as discrete physical objects, and are amenable to quantitative analysis of the interplay between time-dependent eigenmodes and transient disturbance growth. The present approach is partially motivated by recent work on cycle expansions for chaotic systems (e.g., Artuso et al. 1990a,b; Christiansen et al. 1997; Cvitanović et al. 2000), and is related to a recent study based on the Lorenz system (Trevisan and Pancotti 1998).

The model is briefly reviewed in section 2. Section 3 describes the relevant time-dependent basic states, and sections 4 and 5 discuss the Floquet and singular vector analyses, respectively. Section 6 contains discussion, and section 7 summarizes the results.

## 2. Model

The model studied here is a two-layer, $f$-plane, quasigeostrophic fluid in a periodic channel with a rigid lid at the upper boundary, and Ekman dissipation at both upper and lower boundaries. Weakly nonlinear baroclinic wave–mean interaction has been studied in this model by Pedlosky (1971) and Pedlosky and Frenzen (1980), and is summarized in Pedlosky (1987). The model equations and the relevant parameters are summarized here, in notation mostly following the previous references, to which the reader is referred for additional details.

For a weakly supercritical mean flow, a weakly nonlinear disturbance consisting of a single zonal wave component generates a small correction to the mean zonal flow, which in turn affects the growth or decay of the wave. The asymptotic analysis conducted by Pedlosky (1971) yields the coupled system of equations describing this interaction. This system consists of a second-order ordinary differential equation for the wave amplitude $A(t)$, coupled to a partial differential equation for the mean-flow correction $\Psi(y, t)$. If $\Psi$ is expanded in terms of sinusoidal cross-channel modes, the partial differential equation transforms into an infinite set of coupled ordinary differential equations, which may be written

$$\frac{dA}{dt} = -\gamma A + B, \tag{2.1}$$

$$\frac{dB}{dt} = -\frac{1}{2}\gamma B + A\left[1 + \frac{1}{2}\gamma^2 - \sum_{j=1}^{J} a_j(A^2 + V_j)\right], \tag{2.2}$$

$$\frac{dV_j}{dt} = -\gamma(b_j V_j - c_j A^2), \qquad j = 1, 2, \ldots, \tag{2.3}$$

where $J \to \infty$ for the complete expansion, and

$$a_j = \frac{32m^2(2j-1)^2}{[(2j-1)^2 - 4m^2]^2[(2j-1)^2\pi^2 + K^2]}, \tag{2.4}$$

$$b_j = \frac{(2j-1)^2\pi^2}{(2j-1)^2\pi^2 + K^2}, \tag{2.5}$$

$$c_j = 2 - b_j. \tag{2.6}$$

In terms of these variables, the upper- and lower-layer streamfunctions are (to second order in the small parameter $\varepsilon$, whose square measures the supercriticality of the basic steady zonal shear flow)

$$\psi_1(x, y, t) = -\frac{1}{2}U_s y + \varepsilon A(t)\cos kx \sin m\pi y + \varepsilon^2\Psi(y, t), \tag{2.7}$$

$$\psi_2(x, y, t) = +\frac{1}{2}U_s y + \varepsilon\left[A(t)\cos kx + \varepsilon\frac{2m\pi}{U_s}B(t)\sin kx\right] \times \sin m\pi y - \varepsilon^2\Psi(y, t), \tag{2.8}$$

where the mean-flow correction $\Psi(y, t)$ is

$$\Psi(y, t) = \frac{K^2 m}{2U_s}\sum_{j=1}^{J} U_j(t)\frac{\cos[(2j-1)\pi y]}{(2j-1)}, \quad \text{and} \tag{2.9}$$

$$U_j(t) = \frac{8m(2j-1)}{[(2j-1)^2 - 4m^2][(2j-1)^2\pi^2 + K^2]} \times (V_j + A^2). \tag{2.10}$$

Here $K = (k^2 + m^2\pi^2)^{1/2}$ is the total wavenumber of the baroclinic wave, $U_s$ is the mean shear of the basic flow, and $\gamma = r/(2\sigma)$ is the Ekman damping coefficient $\varepsilon r$ scaled by twice the inverse timescale, the small ex-

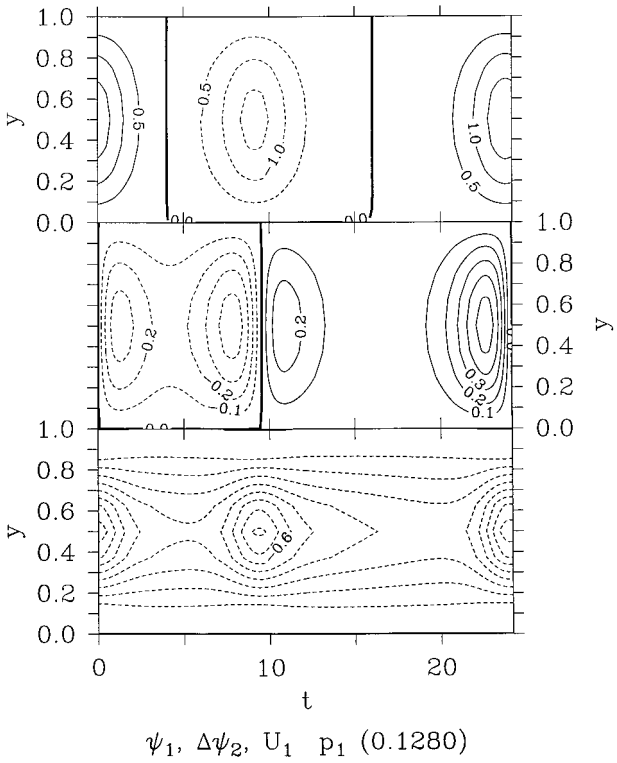


FIG. 1. Limit cycle (stable periodic orbit) for $\gamma = 0.1280$. The cross-channel structure of variables is shown vs time $t$ along the orbit. (Upper panel) $A \sin \pi y$ (the order $\varepsilon$ part of the wave streamfunction at $x = 0$). (Middle panel) $B \sin \pi y$ [order $\varepsilon^2$, proportional to the lower-layer wave streamfunction at $x = \pi/(2k)$]. (Lower panel) $U_{\text{mean}} = \Sigma\, U_j \sin(2j - 1)\pi y$ (proportional to the order $\varepsilon^2$ zonal-flow correction).

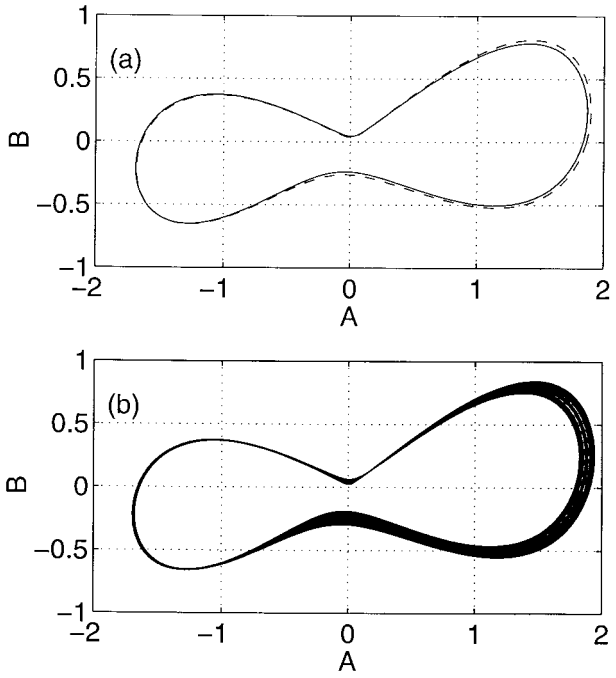


FIG. 2. (a) The projections of the $\gamma = 0.1280$ limit cycle (solid line) and the unstable $\gamma = 0.1315$ period-$T$ cycle (dashed line) on the $A$–$B$ phase plane. (b) The projection of the chaotic attractor for $\gamma = 0.1315$ on the $A$–$B$ phase plane, as represented by a finite segment of a numerical solution.

ponential growth rate $\varepsilon\sigma$ of the linear wave. The channel walls are at $y = \{0, 1\}$. Since $a_j \sim j^{-4}$ as $j \to \infty$, the system may be well approximated numerically by truncating the sums in (2.2) and (2.9) at a finite value $J$, as is done below. A more accurate truncation may be achieved by setting $V_j = V_J$ for $J < j \leq J_1$ in (2.2), with large $J_1$; the sum from $J$ to $J_1$ is then over known coefficients and need be evaluated only once. This truncation is accurate because $b_j$, $c_j \to 1$ as $j \to \infty$, so (2.3) implies that $V_j \to V_\infty$ as $j$, $t \to \infty$ for bounded $|A|$. A brief comparison of these truncations is shown below (Fig. 3), but otherwise the computations use the crude truncation at finite $J$.

Thus, in (2.1)–(2.3), $A$ is the scaled amplitude of the wave, $B$ is a measure of the phase shift between the upper and lower layers (which is of order $\varepsilon^2$), and each $V_j$ represents a scaled combination of zonal-flow component $j$ and the squared wave amplitude. The discussion below primarily refers to the zonal-flow expansion coefficients $U_j$ from (2.9)–(2.10), rather than $V_j$. The form (2.1)–(2.3) is convenient for numerical calculations. Also, it shows immediately that when $\gamma = 0$, the $V_j$ are constants, and (2.1)–(2.2) reduce to an integrable cubic oscillator similar to the Duffing equation, describing a reversible, inviscid wave–mean interaction cycle whose amplitude is determined by initial conditions.

## 3. Periodic orbits

### *a. The $\gamma = 0.1280$ limit cycle*

A numerical exploration of (2.1)–(2.3) has been conducted by Pedlosky and Frenzen (1980). The present study focuses on a set of solutions with $m = 1$ and $K^2 = 2\pi^2$ ($k = \pi$), corresponding to a wave with equal zonal and meridional scales. For these values of $m$ and $K$, the results of Pedlosky and Frenzen (1980, Fig. 3) suggest that solutions of (2.1)–(2.3) undergo a period-doubling transition to chaos near $\gamma = 0.13$. Unless otherwise noted, the results described here were obtained with the simple truncation at $J = 6$ in (2.2). In some cases, slightly different results were obtained for other truncations (see Fig. 3, below) but the main points made here were not affected. Differences between the present numerics and those of Pedlosky and Frenzen (1980) also lead to small but inessential differences in the solutions and their dependence on $\gamma$. A brief summary of other numerical issues is given in the appendix.

For $\gamma = 0.1280$ (and for a range of adjacent $\gamma$; see Fig. 3 below), the numerical solutions approach a limit cycle (Figs. 1, 2a). Let the period of this limit cycle (and its unstable continuation; see below), which depends weakly on $\gamma$, be denoted by $T$; for $\gamma = 0.1280$,

$T \approx 24.176$ (Fig. 1). Note that, since the Eqs (2.1)–(2.3) are unchanged by the transformation $(A, B) \rightarrow (-A, -B)$, an asymmetric cycle is accompanied by a twin of opposite parity, corresponding to an arbitrary along-channel phase shift of a half-wavelength. For simplicity, attention is restricted here to the cycle with parity such that the maximum value of $|A|$ occurs for $A > 0$. Corresponding results for the twin cycle may be obtained by changing the appropriate signs or phases.

In the wave–mean oscillation corresponding to this limit cycle, there is a periodic reduction in zonal shear driven by the growing wave, followed by saturation of wave growth as the source of instability is removed, and subsequent decay of the wave amplitude and resurgence of the zonal shear (Fig. 1; the origin of time is fixed here and below so that $t = 0$ at the point of the cycle where $B = 0$ and $A > 0$). Coriolis forces that arise from the wave-induced meridional circulation drive the changes in zonal flow. The wave amplitude $A$ oscillates between a positive and a negative maximum, each time remaining small for substantial times as it changes sign (Fig. 1). The mean-flow correction reduces the vertical shear everywhere, and is nearly in phase with the squared wave amplitude, consistent with a dominant balance between mean-flow acceleration and potential vorticity fluxes due to secular changes in the wave amplitude, as might be anticipated for small values of friction $\gamma$. Similarly, since $\gamma$ is small, the weakly nonlinear phase shift $B \approx dA/dt$ over most of the cycle, as for the linear modes of instability of the steady zonal flow. The cycle is asymmetric and not sinusoidal. The positive maximum for $A$ is slightly larger than the negative minimum, and the transition from negative minimum to positive maximum takes longer than the reverse. The system evolves relatively slowly near the unstable equilibrium $A = B = U_j = 0$, and $|B|$ is largest for intermediate values of $|A|$ (Figs. 1, 2a).

### *b. Unstable and higher-order cycles ($\gamma = 0.1315$)*

As $\gamma$ increases past 0.1280, the system undergoes a sequence of period-doubling bifurcations. Near $\gamma = 0.1292$, the period-$T$ limit cycle loses stability, and a stable period-$2T$ cycle appears. (Away from the bifurcation point, the ratio of the periods of these two cycles is only approximately 2, but it is customary and useful to continue to identify it as a period-$2T$ cycle, and similarly for the higher-order cycles.) Near $\gamma = 0.1305$, the period-$2T$ cycle loses stability, and a stable period-$4T$ cycle appears. Chaos appears to ensue for $\gamma$ greater than about 0.1309 (Fig. 2b). This sequence is conveniently visualized in a Feigenbaum diagram based on a Poincaré section, in which the value of $A$ when $B = 0$ and $A > 0$ is plotted against $\gamma$ for a set of numerical solutions (Fig. 3a). Near $\gamma = 0.1316$, there is an abrupt change in the solution structure; additional analysis suggests that this change marks the merger of a pair of antisymmetric attractors. More accurate numerical solutions show a similar bifurcation sequence, shifted slightly toward smaller $\gamma$ (Figs. 3b,c).

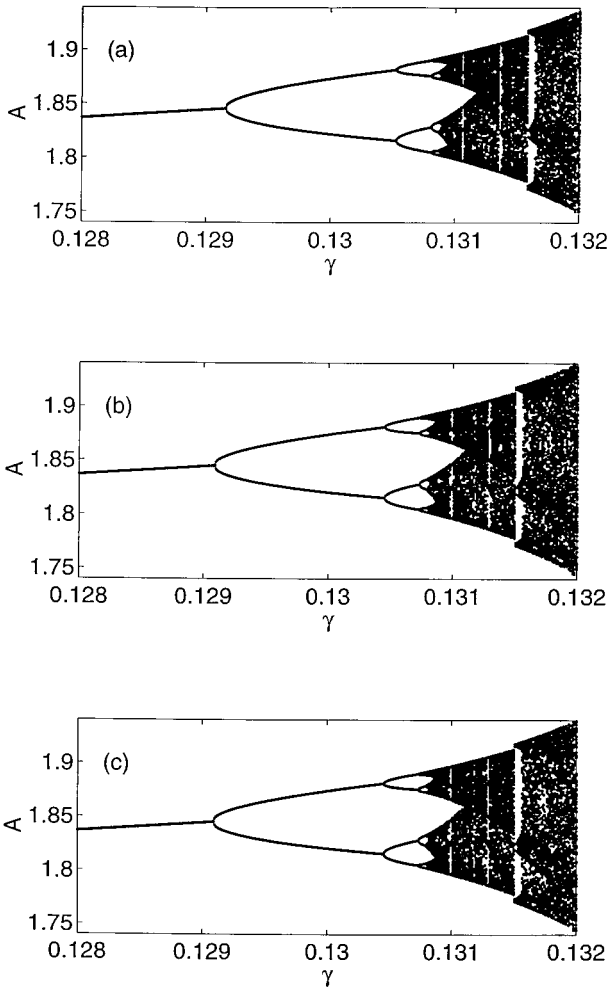


FIG. 3. Feigenbaum diagrams for $0.1280 \leq \gamma \leq 0.132$. This diagram is constructed by plotting the value of $A$ at each time $t > T_0$ at which $B = 0$ and $A > 0$ for numerical solutions at each value of $\gamma$, where $T_0$ is chosen large enough to allow decay of transients. (a) Crude truncation, $J = 6$; (b) crude truncation, $J = 24$; (c) improved truncation, with $J = 6$ and the sum over coefficients approximated by the first 1000 terms. The improved truncation at $J = 6$ gives results that are nearly identical to the crude truncation at $J = 24$.

The periodic orbits that lose their stability in this period-doubling sequence persist as unstable periodic orbits (e.g., Fig. 2a). For $\gamma$ less than about 0.1309, the stable state is a finite-period limit cycle, and the unstable periodic orbits are not directly relevant to the long-time dynamics. In the chaotic regime, however, the set of unstable periodic orbits can be related to the structure of the attractor and the long-time dynamics in a specific, quantitative manner, and may be used to compute statistical averages over the attractor (e.g., Artuso et al. 1990a,b). This relation is only briefly illustrated here, and will be pursued in more detail elsewhere.

For $\gamma = 0.1315$, in the chaotic regime, the evolution

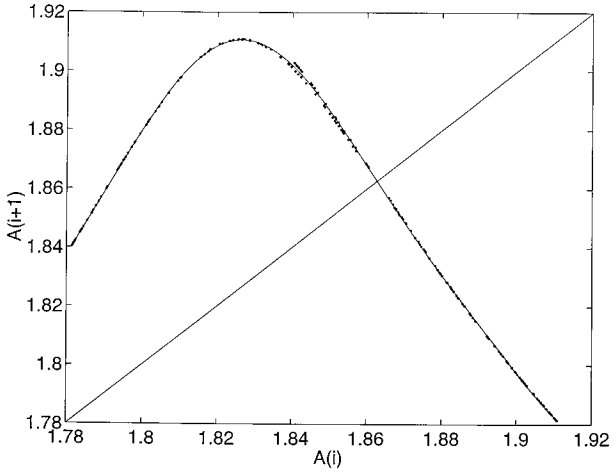


FIG. 4. Numerical Poincaré return map for $\gamma = 0.1315$, constructed by plotting each value of $A$ for $B = 0$ and $A > 0$ against the previous value of $A$ for $B = 0$ and $A > 0$, for a finite segment of a numerical solution. The solid lines are a spline fit to the Poincaré map, and the identity map $F(A) = A$.

may be usefully represented by a one-dimensional map (Fig. 4). From the spline representation of this map, unstable period orbits may be determined systematically in the standard way, by associating the symbols 0 and 1 with the intervals to the left and right, respectively, of the point where the map achieves its maximum, generating a set of binary symbol sequences, and finding the corresponding unique orbit points by inverse iteration. These points may then be used as first guesses for periodic points of the differential equations, which may be improved by a shooting technique that uses Newton's method.

The corresponding unstable cycles for the repeated symbol sequences 1, 10, 1110, 11010, 11110, and 111111111010 are shown in Fig. 5. Because of the geometry of the map, many symbol sequences do not have corresponding cycles. No cycle corresponds to the repeated sequence 0, nor to any sequence containing 00, since all points in the left-hand interval are mapped to points on the right-hand interval (Fig. 4). The unstable cycles "fill out" (more precisely, and under certain conditions that may or may not strictly hold here, are dense on) the attractor (Figs. 5, 2b); it is this property that makes them useful for computing averages.

## 4. Floquet vectors

### *a. Formulation*

Small disturbances to the periodic cycles described in the previous section will satisfy a linearized form of (2.1)–(2.3), in which the given periodic cycle is the time-dependent basic state about which the equations are linearized. The solutions of the corresponding linearized equations may be computed by standard techniques for linear differential systems with periodic coefficients (e.g., Coddington and Levinson 1955), often known as Floquet theory. For a periodic orbit solution $P(t) = [A(t), B(t), U_1(t), U_2(t), \ldots, U_J(t)]$, any linear disturbance may be written as a fixed sum of the $J + 2$ Floquet eigenvectors $\{\boldsymbol{\phi}_j(t), j = 1, 2, \ldots, J + 2\}$,

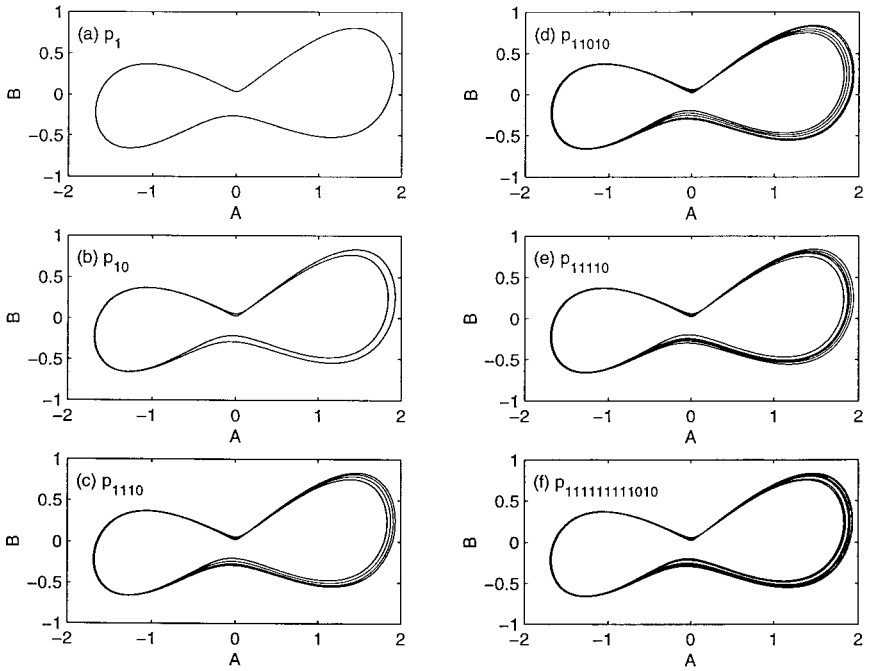


FIG. 5. Unstable cycles for $\gamma = 0.1315$: (a) $p_1$, period $T$; (b) $p_{10}$, period $2T$; (c) $p_{1110}$, period $4T$; (d) $p_{11010}$, period $5T$; (e) $p_{11110}$, period $5T$; (f) $p_{111111111010}$, period $12T$.

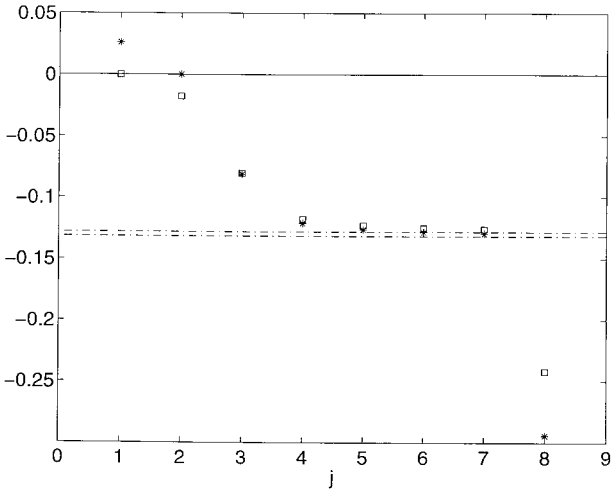


FIG. 6. Floquet exponents $\lambda_j$, $j = 1, \ldots, 8$, for the $\gamma = 0.1280$ (squares) and $\gamma = 0.1315$ (stars) period-$T$ cycles, ordered by decreasing exponent. The dashed lines indicate the corresponding values of $-\gamma$.

where (for nondegenerate systems) each vector has the form $\boldsymbol{\phi}_j = \boldsymbol{\Phi}_j(t) \exp(\lambda_j t)$, for a $(J + 2)$-component vector function $\boldsymbol{\Phi}_j(t)$, with $\boldsymbol{\Phi}_j(t + T) = \boldsymbol{\Phi}_j(t)$ [or possibly $\boldsymbol{\Phi}_j(t + T) = -\boldsymbol{\Phi}_j(t)$]. Each $\boldsymbol{\phi}_j$ is a solution of the linearized equations around the given cycle.

Here, attention is restricted to the shortest cycles, the unstable period-$T$ cycle for $\gamma = 0.1315$ and the stable period-$T$ cycle for $\gamma = 0.1280$. These two cycles are very similar (Fig. 2a; see also Figs. 1 and 9a, below), with nearly indistinguishable spatial and temporal wave and mean-flow structure, the main difference being only that one cycle is stable and the other slightly unstable. The corresponding periods $T$ are $T = 24.176$ for $\gamma = 0.1280$ and $T = 24.479$ for $\gamma = 0.1315$. The Floquet problems were solved numerically, as described in the appendix.

### b. Results

The Floquet characteristic exponents $\lambda_j$ for these two cycles are shown in Fig. 6. Positive exponents indicate instability, and negative indicate stability. The solutions are obtained for the truncation $J = 6$, so there are eight Floquet eigenvectors. Some of the corresponding structure functions $\boldsymbol{\Phi}_j$ for $\gamma = 0.1280$ are shown in Fig. 7. The Floquet vectors essentially divide into two types. The neutral vector ($\boldsymbol{\phi}_1$ for $\gamma = 0.1280$, or $\boldsymbol{\phi}_2$ for $\gamma = 0.1315$) is proportional at each point of the cycle to the rate of change along the cycle, and so describes wave-dynamical processes, as does the oscillation itself. The least and most stable nonneutral Floquet vectors ($\boldsymbol{\phi}_2$ and $\boldsymbol{\phi}_8$ for $\gamma = 0.1280$, or $\boldsymbol{\phi}_1$ and $\boldsymbol{\phi}_8$ for $\gamma = 0.1315$) are also of this type, as they each differ in structure from the neutral vector essentially only by a change in phase at minima of $|A|$ and an exaggerated asymmetry between the maxima in the unstable mode, relative to the neutral mode (Figs. 7a,b,d). In contrast, $\boldsymbol{\phi}_4$–$\boldsymbol{\phi}_7$ have mean-flow structure dominated by higher meridional harmonics (Fig. 7c). These modes have decay rates nearly equal to $\gamma$, and evidently describe the frictional decay of the higher mean-flow harmonics. The vector $\boldsymbol{\phi}_3$, which has intermediate stability, appears to be a mixture of these two types.

The decaying wave-dynamical mode $\boldsymbol{\phi}_8$ distinguishes itself from the corresponding least stable nonneutral wave-dynamical mode ($\boldsymbol{\phi}_2$ or $\boldsymbol{\phi}_1$) by its larger amplitude during the decay phase that follows each wave maximum along the basic-state wave–mean cycle. This distinction can be seen by comparing the wave or mean-flow disturbances in Figs. 7b and 7d immediately before and after each wave amplitude maximum in Fig. 1. The sustained disturbance growth or decay described by the wave-dynamical Floquet vectors is accomplished by this asymmetry in the disturbance oscillations.

The dynamical splitting into two types of modes is evident also in the disturbance heat (or potential vorticity) flux associated with these cycles. An appropriate heat flux quantity is the cycle average of the product $\boldsymbol{\Phi}_A \boldsymbol{\Phi}_B$, the first two components of $\boldsymbol{\Phi}_j$, for each $j$. For both cycles, this quantity is of order $10^{-2}$ for $\boldsymbol{\phi}_1$–$\boldsymbol{\phi}_3$; $-10^{-2}$ for $\boldsymbol{\phi}_8$; and $10^{-5}$, $10^{-6}$, $10^{-7}$, $10^{-8}$ for $\boldsymbol{\phi}_4$–$\boldsymbol{\phi}_7$, respectively. Thus, the wave-dynamical modes have much larger heat fluxes than the decaying zonal flow modes; the heat flux is large but countergradient for the rapidly decaying wave-dynamical mode $\phi_8$.

This dynamical splitting persists for the higher-order $\gamma = 0.1315$ cycles. Characteristic exponents for 138 of these cycles, ordered by symbol sequence, exhibit substantial variations for the least and most unstable modes, and for the third mode, and very little variation for modes 4 through 7 (Fig. 8). The variations in the exponents compensate, as they must, since the sum of the exponents equals the trace of the Jacobian matrix; numerically these sums were equal and constant to $10^{-7}$ or less, while the neutral eigenvalue was numerically of order $10^{-6}$ or less. The eigenvectors for $\gamma = 0.1280$ and $\gamma = 0.1315$ are very similar, as can be anticipated from the similarity of the cycles (Figs. 1, 2a, and 9a). The unstable vector ($\boldsymbol{\phi}_1$) for $\gamma = 0.1315$ is similar to the least stable nonneutral vector ($\boldsymbol{\phi}_2$) for $\gamma = 0.1280$, with a modest change in the relative magnitude of the wave amplitude peaks (Figs. 7a, 9b); the bifurcation to instability of the cycle as $\gamma$ varies is associated with the change in sign of the Floquet exponent for this vector.

### c. The bred growing mode analogy

The Floquet vectors are the simplest analog of the bred growing modes (BGMs; Toth and Kalnay 1997) used for ensemble generation in operational forecast models. As noted above, bred growing modes are com-

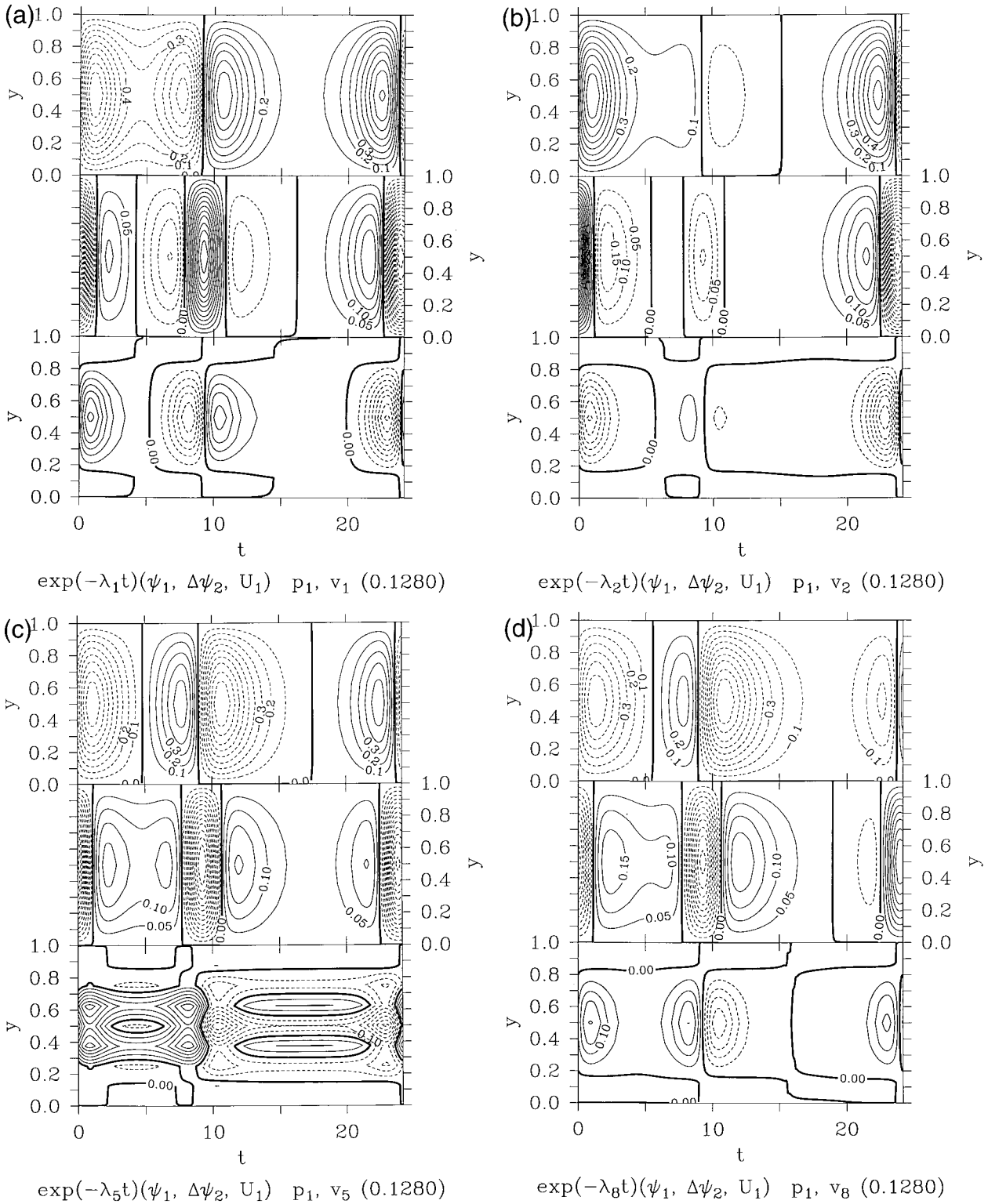


FIG. 7. Time-dependent physical fields corresponding to the Floquet eigenvector structure functions $\mathbf{\Phi}_j(t)$, ordered as in Fig. 6, for the $\gamma = 0.1280$ cycle. The corresponding Floquet eigenvectors are $\boldsymbol{\phi}_j = \exp(\lambda_j t)\mathbf{\Phi}_j$. The format is as in Fig. 1, except that each panel shows the corresponding linear disturbance variable: (a) $\mathbf{\Phi}_1$, the neutral vector, proportional to the rate of change along the limit cycle; (b) $\mathbf{\Phi}_2$; (c) $\mathbf{\Phi}_5$; (d) $\mathbf{\Phi}_8$.

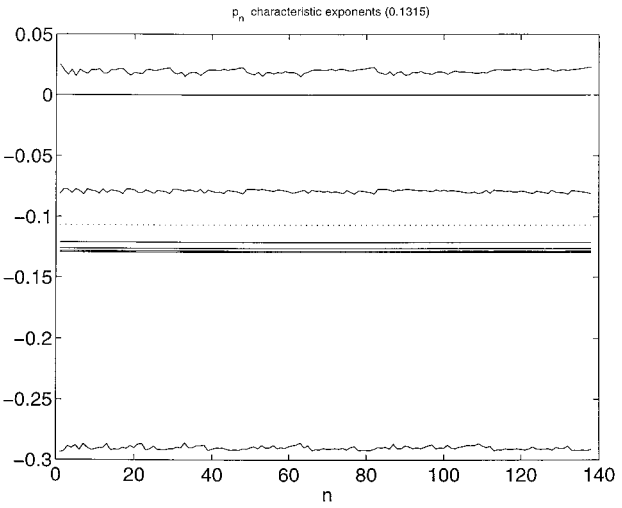


FIG. 8. Floquet exponents $\lambda_j^{(n)}$ for 138 unstable periodic cycles $p_n$ for $\gamma = 0.1315$. The dashed line is the sum of the eight exponents for each cycle (equal to the trace of the Jacobian matrix), divided by 8. Six of these 138 cycles are shown in Fig. 5.

puted by an iterated breeding cycle, in which the differences between forecast ensemble members and a control forecast is rescaled and added to the analysis at each analysis cycle to initialize a new ensemble. In the simplest idealization, in which only linear disturbances are permitted and no additional model of the forecast–analysis cycle is included, the Floquet vectors (or suitably orthogonalized combinations thereof) may be viewed as analogs of the modes that one may expect eventually to emerge from a BGM iteration for a control forecast corresponding to the periodic basic state. (For a nonperiodic basic state, the idealized analogs of BGMs are Lyapunov vectors.)

For the stable ($\gamma = 0.1280$) cycle, all disturbances decay except those that are tangent to the cycle. The resulting BGM-analog disturbance is a time-dependent phase shift along the cycle, which is described in the linear approximation by the neutral Floquet vector. A corresponding BGM-analog ensemble would itself oscillate periodically, spreading exponentially along the cycle during the exponential growth phase of the cycle, and contracting exponentially during the decay phase. Thus, in spite of its overall long-term stability, the time-dependent flow will have a nontrivial BGM analog that is associated with the cyclic growth and decay of the baroclinic wave. The local oscillation of disturbance amplitude that is described by the neutral Floquet vector is due to precisely the same process that causes the oscillation of the wave amplitude itself, not an additional or secondary oscillation or instability. The growth of disturbances is a direct consequence of the growth of the time-dependent basic state. It can be inferred that any time-dependent state will induce a similar type of disturbance growth during its periods of growth.

For the unstable ($\gamma = 0.1315$) cycle, one of the Flo-

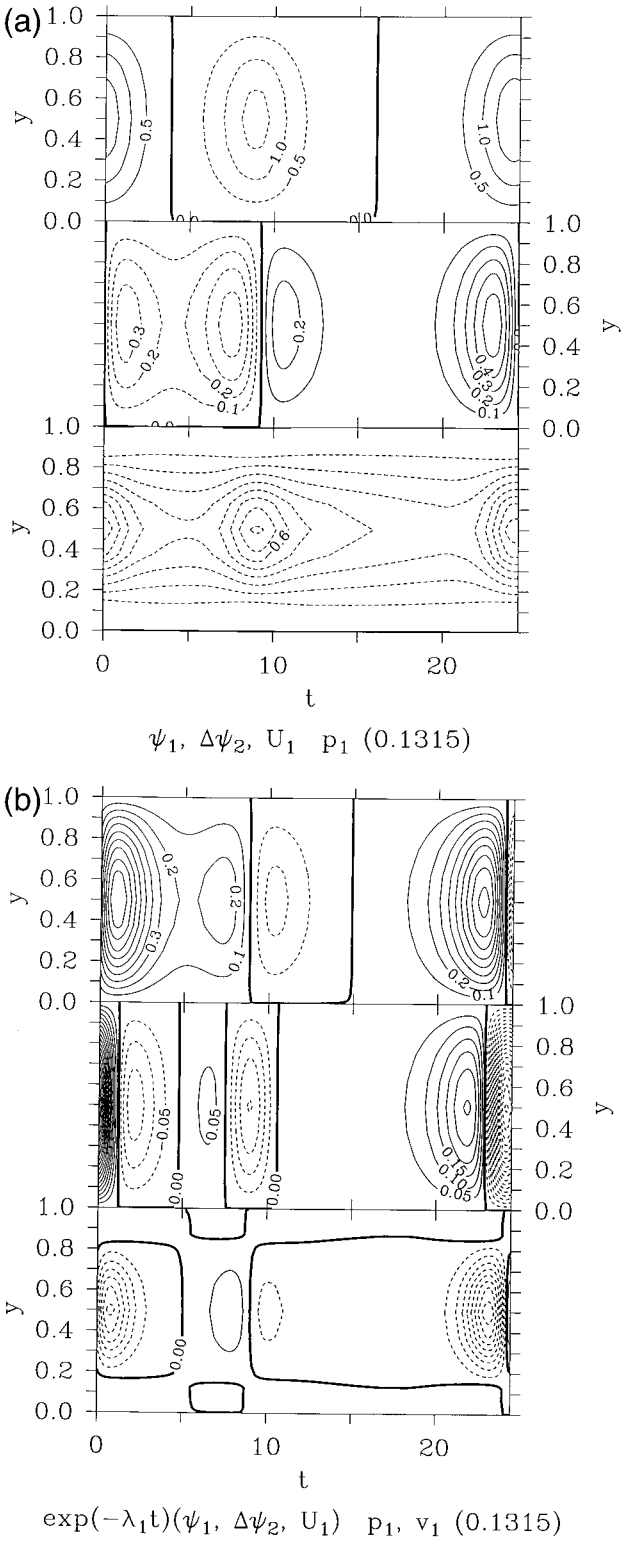


FIG. 9. (a) As Fig. 1, but for the $\gamma = 0.1315$ period-$T$ cycle. (b) As Fig. 7a, but for the first Floquet vector $\mathbf{\Phi}_1$ of the $\gamma = 0.1315$ period-$T$ cycle.

quet exponents in positive, and the corresponding disturbance will grow exponentially. This mode supplies a second BGM analog, in addition to the neutral mode. However, the positive Floquet exponent is roughly 0.025, 40 times smaller than the growth rate of the baroclinic instability and the inverse timescale of the basic baroclinic oscillation. Thus, the disturbance growth processes that are relevant on the baroclinic wave timescale are still primarily associated with the growth and decay phases of the oscillation itself, rather than with this additional weak time-dependent instability.

If attention is extended to the nonperiodic attractor indicated by the $\gamma = 0.1315$ numerical solutions, the unstable Floquet vector of the period-$T$ cycle provides additional information, as the large-scale structure of the attractor tends to be tangent to this unstable eigenvector (Fig. 10). Since the attractor is in general a fractal object (Fig. 10), the precise meaning of the phrase ''tangent to the attractor's large-scale structure'' is not easily understood, but in practice it is useful if the large-scale geometry is sufficiently simple. For example, in Fig. 10, both the large-scale structure and the disturbance along $\boldsymbol{\phi}_1$ (and, in this case, also those along $\boldsymbol{\phi}_2$ and $\boldsymbol{\phi}_8$) lie on the diagonal from upper left to lower right. Thus, in this case, the BGM analog can give an indication of the distribution of dynamically accessible states near the unstable periodic orbit that would be relevant to ensemble construction for this idealized model.

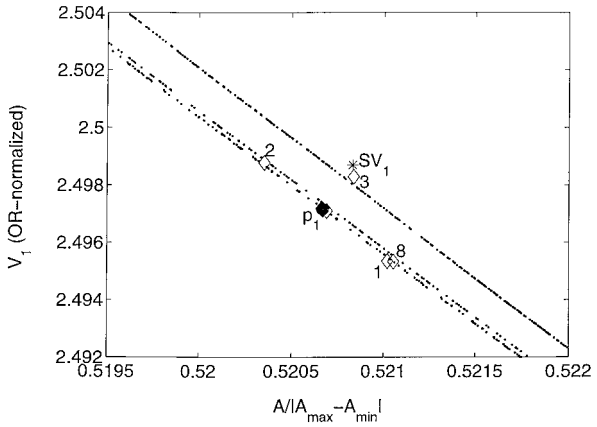


FIG. 10. Attractor structure and linear disturbances on the Poincaré section $B = 0$ and $A > 0$, projected on the $A$–$V_1$ plane and with $A$ and $U_1$ normalized by orbit excursions as for the OR norm. The unstable period-$T$ orbit (large dot with adjacent label $p_1$) and points on the attractor from a numerical solution (small dots) are marked, along with the projections of disturbances from the unstable period-$T$ orbit $p_1$ along Floquet eigenvectors 1, 2, 3, and 8 (numbered diamonds), and the projection of a disturbance from $p_1$ along the first singular vector (star with label $SV_1$). The disturbances of equal amplitude along Floquet vectors 4–7 are small in projection and cluster near $p_1$.

## 5. Singular vectors

### a. Formulation

The Floquet vectors give a complete description of the behavior of linear disturbances, and identify the disturbances of fixed spatiotemporal structure that will grow or decay at fixed exponential rates over the course of a period. Alternatively, it is possible to inquire which linear disturbances are maximally amplified after a fixed interval of time (Lorenz 1965; Farrell 1989). Such optimal disturbances, referred to here as singular vectors (SVs), generally exhibit transient growth, and do not have fixed modal structure.

Let $\boldsymbol{\xi}(t) = [\xi_1(t), \xi_2(t), \ldots, \xi_{J+2}(t)]$ represent an arbitrary linear disturbance to the periodic orbit, and let $\mathcal{N}_1(\boldsymbol{\xi}) = \hat{\mathcal{N}}_1(\boldsymbol{\xi}, \boldsymbol{\xi})$ and $\mathcal{N}_2(\boldsymbol{\xi}) = \hat{\mathcal{N}}_2(\boldsymbol{\xi}, \boldsymbol{\xi})$ denote the initial and final norms, respectively, with respect to which the amplitude of the disturbance is to be computed, where

$$\hat{\mathcal{N}}_1(\boldsymbol{\xi}, \boldsymbol{\xi}') = \boldsymbol{\xi}^{\mathrm{T}}\mathbf{N}_1\boldsymbol{\xi}', \qquad \hat{\mathcal{N}}_2(\boldsymbol{\xi}, \boldsymbol{\xi}') = \boldsymbol{\xi}^{\mathrm{T}}\mathbf{N}_2\boldsymbol{\xi}' \quad (5.1)$$

are the associated inner products. Here $\mathbf{N}_1$ and $\mathbf{N}_2$ are (symmetric) weighting matrices, and the superscript T denotes transpose. Then the SVs are the vectors $\boldsymbol{\xi}(t_1)$ that maximize $\mathcal{N}_2[\boldsymbol{\xi}(t_2)]$, subject to $\mathcal{N}_1[\boldsymbol{\xi}(t_1)] = 1$.

Since the Floquet vectors span the phase space, the disturbance $\boldsymbol{\xi}(t)$ may be written as a sum of Floquet vectors,

$$\boldsymbol{\xi}(t) = \sum_{j=1}^{J+2} a_j\boldsymbol{\phi}_j(t) = \mathbf{Z}(t)\mathbf{a}, \quad (5.2)$$

where $\mathbf{Z}(t) = [\boldsymbol{\phi}_1(t), \boldsymbol{\phi}_2(t), \ldots, \boldsymbol{\phi}_{J+2}(t)]$ is the matrix whose columns are the Floquet vectors $\boldsymbol{\phi}_j$. The expansion coefficient vectors $\mathbf{a} = [a_1, a_2, \ldots, a_{J+2}]$ are independent of time, so if the $\boldsymbol{\Phi}_j$ and $\lambda_j$ are known, it suffices to determine the $\mathbf{a}$ at the initial time $t_1$ in order to compute $\boldsymbol{\xi}(t)$ for any $t$. Define the ''linear propagator'' $\mathcal{L}(t_1, t) = \mathbf{Z}(t)\mathbf{Z}(t_1)^{-1}$, in terms of which $\boldsymbol{\xi}(t) = \mathcal{L}(t_1, t)\boldsymbol{\xi}(t_1)$. Then the SV maximization yields the generalized eigenvalue problem

$$[\mathcal{L}(t_1, t_2)]^{\mathrm{T}}\mathbf{N}_2\mathcal{L}(t_1, t_2)\boldsymbol{\xi}(t_1) = \mu^2\mathbf{N}_1\boldsymbol{\xi}(t_1) \quad (5.3)$$

for the SVs in the usual way (e.g., Buizza et al. 1993). The matrices $\mathbf{Z}$ and $\mathcal{L}$ may be calculated directly from the Floquet vectors $\boldsymbol{\phi}_j$ at the initial ($t_1$) and final ($t_2$) times. The eigenvalue problem (5.3) may then be solved by standard methods for the eigenvector–eigenvalue pairs $\{(\boldsymbol{\xi}^l, \mu_l^2), l = 1, \ldots, J + 2\}$. From (5.2), the Floquet decompositions of the SVs are then $\mathbf{a}^l = \mathbf{Z}^{-1}(t_1)\boldsymbol{\xi}^l$. The square root $\mu_l$ of each eigenvalue is the corresponding singular value.

For a given periodic orbit $p$, the SVs depend on the initial and optimization times $t_1$ and $t_2$, and on the norms defined by the matrices $\mathbf{N}_1$ and $\mathbf{N}_2$. Since the periodic orbits have been determined numerically, analytical solutions for the SVs are not available, and the SVs must be calculated numerically, which requires that specific choices for these quantities be made. Attention is restricted here to two simple choices for $\mathbf{N}_1$ and $\mathbf{N}_2$, while the dependence of the corresponding SVs on $t_1$ and $t_2$ is explored more completely.

The two choices of norm are referred to here as the ''orbit-relative'' (OR) and ''amplitude energy'' (AE) norms. For convenience, the matrices $\mathbf{N}_1$ and $\mathbf{N}_2$ are taken equal in each case. Since the initial and final norms are then equivalent, the singular values $\mu_l$ are amplification factors. This restriction is not necessary, but simplifies the interpretation. In both cases, $\mathbf{N}_1$ and $\mathbf{N}_2$ are also taken to be diagonal matrices. For the AE norm, $\mathbf{N}_1$ and $\mathbf{N}_2$ are the identity matrix, so the norm is simply the sum of squares of the disturbance amplitudes $\boldsymbol{\xi}_j$. In terms of the physical variables, this is closely related to the usual energy, except that terms of first and second order in the small-amplitude parameter $\varepsilon$ are weighted equally. A similar norm would be obtained by computing the usual energy and formally setting $\varepsilon = 1$ in (2.7)–(2.8), so the AE norm is essentially a physical energy norm based on extrapolation of the small-amplitude results to finite amplitude. For the OR norm, the $j$th diagonal element in $\mathbf{N}_1$ and $\mathbf{N}_2$ is the inverse square of the peak-to-peak amplitude excursion of the $j$th component of the periodic orbit solution. That is, the linear disturbance of each component is measured relative to the magnitude of the variation of the corresponding component along the periodic orbit. Because higher mean-flow components $U_j$ have relatively small variation along the periodic orbit, the OR norm gives them greater weight than does the AE norm.

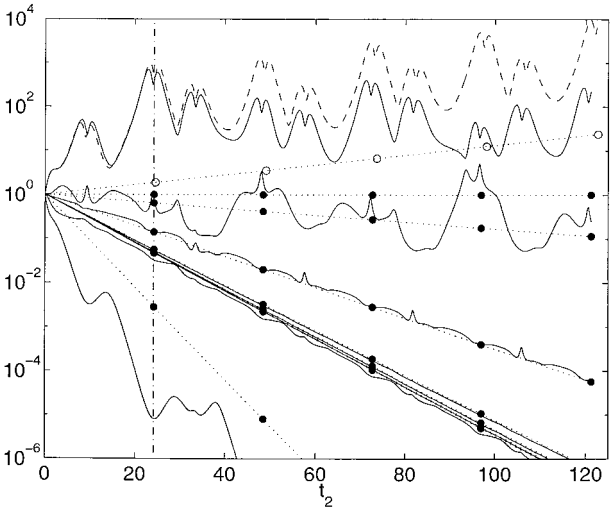


FIG. 11. Singular values (solid lines) as a function of $t_2$ (or, equivalently, of $\tau = t_2 - t_1$) along the $\gamma = 0.1280$ limit cycle for $t_1 = 0$ and the OR norm, for $0 \le t_2 \le 5T$, with the mean decay $\exp(\lambda_j t_2)$ of the Floquet vectors for the corresponding times (dotted lines); at each integral period $t_2 = nT$ (large dots), the latter correspond to the ratio of the instantaneous and initial Floquet vector amplitudes. The time $t_2 = T = 24.176$ is indicated (dash–dot line). The leading singular value (dashed line) and the mean growth $\exp(\lambda_1 t_2)$ for the first Floquet vector (dotted line with open circles) for the $\gamma = 0.1315$ unstable period-$T$ cycle (for which $T = 24.479$) are also shown for comparison.

*b. Results*

Singular vectors are computed for the stable cycle at $\gamma = 0.1280$ and for the period-$T$ unstable cycle at $\gamma = 0.1315$. The dependence of the SVs on initialization time $t_1$ and final time $t_2$ is investigated, for both fixed-length (variable $t_1$, constant $\tau = t_2 - t_1$) and variable-length (constant $t_1$, variable $\tau$) optimization intervals. As above, the calculations are done for the truncation $J = 6$, so each yields 8 SVs. Although there are quantitative differences between the results for the two norms, qualitatively the results are similar.

For $\gamma = 0.1280$, the OR-norm SVs for $t_1 = 0$ (Fig. 11) divide into two classes, as did the Floquet vectors. The first and last SVs (in order of decreasing singular value) rapidly amplify and decay, respectively, in each case more rapidly than the corresponding Floquet vector. The singular value for the first SV, $\mu_1$, depends strongly on the optimization interval $\tau = t_2 - t_1 = t_2$, and is relatively large where the wave amplitude of the periodic cycle is large, and relatively small where the wave amplitude is small (Fig. 11). The maximum value of $\mu_1$ for $0 < t_2 < T$ is approximately 800, near $t_2 = 23$. On longer timescales, $\mu_1$ continues to oscillate with $t_2$, in phase with the wave amplitude, but never exceeds 800. This bounded amplification is consistent with the stability of the $\gamma = 0.1280$ periodic orbit. The fluctuations in $\mu_2$ appear to grow with time, at least during the period $0 < t_2 < 5T$. The intermediate SVs have amplification factors that correspond closely to the decay rates of the intermediate Floquet vectors. Thus, the dynamical splitting of the Floquet vectors into wave-dynamical modes and decaying zonal-flow modes is also reflected in the SVs.

The first SV is primarily a combination of the two wave-dynamical Floquet vectors, $\boldsymbol{\phi}_2$ and $\boldsymbol{\phi}_8$, plus a contribution from the neutral vector $\boldsymbol{\phi}_1$. Despite the strong dependence of $\mu_1$ on $t_2$ (or, equivalently, on the optimization interval $\tau$) for $t_1 = 0$, the Floquet decomposition $\mathbf{a}^1$ of the first SV is nearly independent of $t_2$, as the ratios $|a_j^1|/|\mathbf{a}^1|$ for the dominant components $a_j^1$ of the first SV change by only a few percent for $0 < t_2 < T$. The Floquet vectors themselves are strongly time-dependent, so the final physical structure of this SV depends strongly on $t_2$, and only the Floquet decomposition is nearly independent of $t_2$.

When $t_1$ varies (for fixed optimization interval $\tau$), the singular values $\mu_l$ continue to split in the same way, and $\mu_1$ oscillates in the same way, with maxima where $t_2$ corresponds to maxima in the wave amplitude for the basic cycle (Fig. 12a). The Floquet decomposition of the first SV depends more strongly on $t_1$ with fixed $\tau$ (Fig. 12b) than on $t_2(\tau)$ with fixed $t_1$. The wave-dynamical and neutral Floquet vectors still dominate the first SV, but there are rapid oscillations with $t_1$ in the relative proportion of these contributions during periods where the wave amplitude is small ($t_1 \approx 5$, $t_1 \approx 20$). Elsewhere in the cycle, however, the decomposition in terms of Floquet vectors is often independent of $t_1$ for

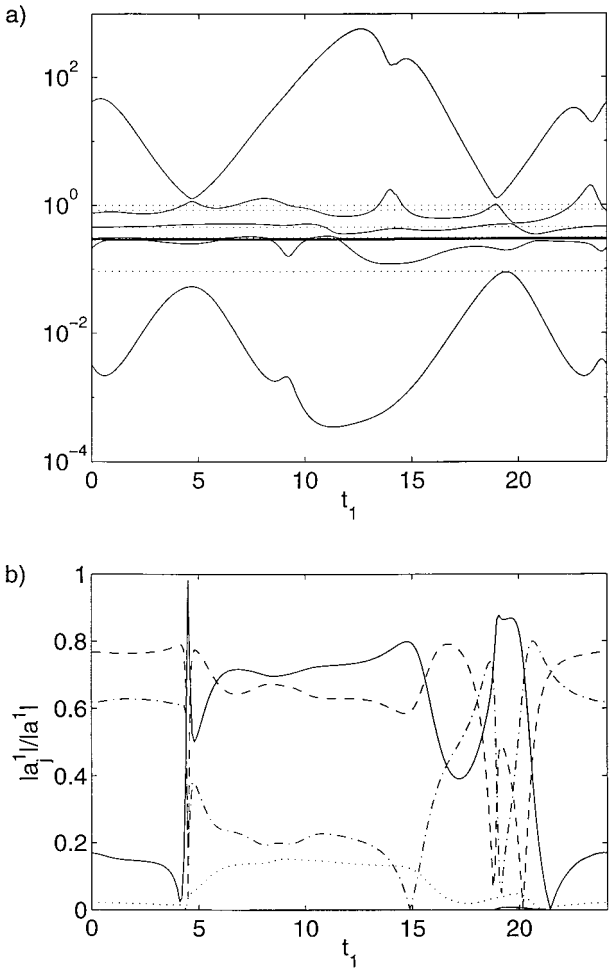


FIG. 12. (a) Singular values (solid lines) as a function of $t_1$ along the $\gamma = 0.1280$ limit cycle for fixed $\tau = t_2 - t_1 = 100\delta t \approx t_1 + 10$ and the OR norm, with the corresponding mean Floquet decays $\exp(\lambda_j \tau)$ (dotted lines). (b) Floquet vector components $a_1^1$ (solid line), $a_2^1$ (dashed), $a_3^1$ (dotted), $a_8^1$ (dash–dot), of the leading singular vector $\mathbf{a}^1$ vs $t_1$ for fixed $\tau = t_2 - t_1 = 100\delta t \approx 10$ and the OR norm. Components 4–7 are also shown (solid) but are generally small.

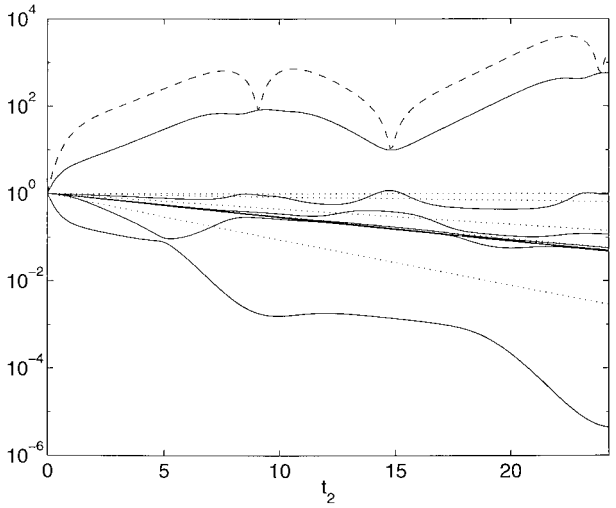


FIG. 13. Singular values (solid lines) and mean Floquet decays (dotted) for $\gamma = 0.1280$ as in Fig. 11, but for the AE norm and for $0 \le t_2 \le T$ only. The leading singular value for the SE norm is also shown (dashed).

substantial periods. During these periods, the corresponding physical structure of the first SV can change rapidly and dramatically. For example, during the interval $6 < t_1 < 13$, the Floquet decomposition is nearly fixed (Fig. 12b), but the Floquet vectors change markedly (Fig. 7), as the $A$ and $B$ components sequentially pass through zero crossings, implying rapid changes in the physical structure of the first SV.

Additional SV solutions for other values of $t_1$ and $t_2$, for fixed-length intervals with different $\tau$ and for variable-length intervals with different $t_1$, confirm these general tendencies: the amplification factor $\mu_1$ oscillates with $t_2$, in phase with the wave amplitude of the cycle; and the Floquet decomposition $\mathbf{a}^1$ primarily involves the wave-dynamical and neutral vectors, and is relatively independent of $t_2$ when $t_1$ is near the phase of maximum wave amplitude (or when $t_2$ is large), and strongly dependent on $t_1$ and $t_2$ when $t_1$ is near the phase of minimum wave amplitude. For the AE norm, the dependence of the amplification factors on $t_1$ and $t_2$ is qualitatively similar, though quantitatively different (Figs. 13, 14a). The decomposition $\mathrm{a}^1$ is still dominated by the wave-dynamical and neutral Floquet vectors, but the dependence of the decomposition on $t_1$ is relatively stronger (Fig. 14b).

For the unstable cycle at $\gamma = 0.1315$, the results are much the same. This can be anticipated from the similarity of the cycles themselves, and of the Floquet vectors and exponents, and the relatively long timescale of the instability ($1/\sigma \approx 40$) relative to the baroclinic wave timescale. The major difference is that, on long timescales, the leading SV amplification factor $\mu_1$ tends to increase at an exponential rate equal to the leading Floquet exponent, as should be expected (Fig. 11). The Floquet vector decomposition of the leading SV has the same structure as for $\gamma = 0.1280$, with contributions primarily from the wave-dynamical and neutral vectors.

Some singular vectors were computed for a third, scaled physical energy norm, which was equivalent to the AE norm except that the second-order quantities $B$ and $U_j$ were scaled by $\varepsilon = 0.01$, corresponding roughly to a physical energy for a small but finite-amplitude disturbance. The qualitative results were again generally similar (Fig. 13, dashed line).

As noted above, the leading Floquet vector of an unstable cycle in a chaotic regime tends to be tangent, in some large-scale sense, to the attractor. Because of the contributions from other vectors, the leading SV does not generally share this property. This suggests that, to the extent that prediction errors are due solely to errors in estimating the initial conditions on the attractor, as they will be if the model attractor accurately describes

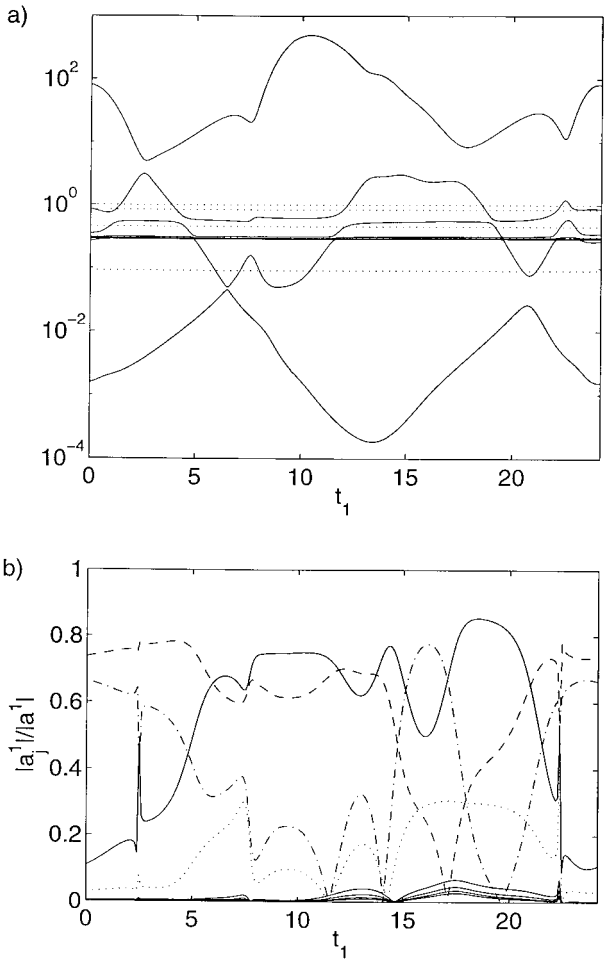


FIG. 14. As Fig. 12, but for the AE norm.

the dynamically accessible states, the leading SV will in general be irrelevant to the predictability of the nonlinear system, since the disturbances it describes will evidently be dynamically inaccessible. However, if the attractor is examined on smaller scales, its fractal structure becomes apparent, and a leading SV disturbance may apparently still lie on the attractor (Fig. 10). This illustrates that inferences about the accessibility of states described by Floquet vectors (or BGMs) and SVs in an idealized model such as this one rely on the simple geometric structure of the model attractor, and may not easily generalize to more complex models. If model error is such that the dynamically accessible states are not accurately described by the attractor, then of course such inferences also do not follow.

## 6. Discussion

The Floquet vector analysis illustrates that, in this highly constrained model of baroclinic wave–mean dynamics, disturbance growth and decay on the wave timescale are dominated by the wave growth and decay processes that give rise to the basic-state oscillation. This is true even in the unstable ($\gamma = 0.1315$) case, since the Floquet instability is weak, with growth timescale much longer than the wave growth timescale. The neutral Floquet vector, which corresponds to phase shifts along the cycle, always gives rise to a nontrivial bred growing mode analog. This mode describes disturbance growth and decay that arise purely from the wave growth and decay processes associated with the basic-state oscillation.

For the singular vectors, more rapid transient amplification is possible, primarily during the first wave growth events encountered by the disturbance. This transient growth clearly arises from nonorthogonality of the Floquet vectors with respect to the inner products considered here, as it could not otherwise exceed the growth of the leading Floquet vector. In the long-term average, the transient growth eventually halts for the stable ($\gamma = 0.1280$) case, but does not decay. The finite asymptotic growth arises from the existence of disturbances corresponding to phase shifts along the cycle, which are neutral in the long-term average. In contrast, transient linear disturbances to steady flows generally decay after amplifying. In the unstable case, the transient growth eventually asymptotes toward exponential growth at the rate of the leading Floquet vector, as it must.

The Floquet vectors divide into two sets, the first including two wave-dynamical vectors and the neutral vector, and the second containing vectors associated with the decaying, high meridional modes of the zonal flow. Thus, despite the constraints that arise from the exact time periodicity of the basic state, which might be anticipated to impose artificial characteristics on the solutions, the natural modes of the eigenvalue problem reflect identifiable physical processes in an appealing way. In addition, this splitting is associated with a tendency toward orthogonality (for the inner products considered here) between the wave-dynamical modes and the decaying modes. This orthogonality is clear for linearization about the zero state ($A = B = U_j = 0$), but need not persist for linearization about the time-dependent states.

One manifestation of this orthogonality is the corresponding split in the composition of the singular vectors. The leading singular vector is dominated by the wave-dynamical and neutral Floquet vectors, while intermediate decaying singular vectors closely follow the decay of the intermediate Floquet vectors. This split occurs because orthogonal, or nearly orthogonal, vectors cannot be effectively combined to induce nonmodal transient amplification. The Floquet vectors, and thus their dynamical splitting, are independent of the norm used to measure the amplitude of disturbances. In contrast, the singular vectors depend on this norm. The results described here indicate that the dynamical splitting of the Floquet vectors is sufficiently robust that

reasonable choices of norm preserve this splitting in the singular vectors, to a recognizable degree.

The approximate constancy of the Floquet vector decompositions of the leading singular vector as a function of initial ($t_1$) and optimization ($t_2$) times, for substantial segments of the cycles, was an unexpected result. It evidently indicates that individual Floquet vectors capture essential aspects of disturbance evolution even over partial cycles, during which the periodic character of the time-dependent basic state is not yet apparent. In this sense, the Floquet vectors appear to be physically more meaningful than might have been anticipated. It also also indicates a rigidity of the asymptotic dynamics, in which the relative orientation of the Floquet vectors in phase space tends to persist for timescales associated with the basic-state wave growth and decay. This is presumably related to the presence of a single dominant physical instability in the model, the baroclinic instability of the basic zonal shear flow at the fixed wavenumber $k$.

Some aspects of these results appear consistent, in a general sense, with results from more complex models. For example, Vannitsem and Nicolis (1997) find that growing Lyapunov vectors (the analog of Floquet vectors for nonperiodic states) in a 3-layer quasigeostrophic numerical model tend to have wavenumber spectra that peak at synoptic scales, while decaying vectors have greater variance at smaller and larger scales, suggesting a broadly similar dynamical split between growing and decaying vectors that are distinguished by spatial structure. Buizza and Palmer (1995) analyze singular vectors from an operational global numerical weather prediction model. They find that growing singular vectors tend to have maximum amplitude in regions where the local value of the expression for the Eady growth rate is large, suggesting a link between baroclinic wave dynamics and growing singular vectors, but also find evidence of nonmodal growth in the leading singular vectors. These findings are also broadly consistent with the behavior of the present, idealized model. However, there are many important differences. The large number of amplifying Lyapunov and singular vectors, respectively, in the more complex models is a significant difference from the present model, in which at most one Floquet or singular vector shows substantial amplification. It has been argued above that the primary mechanism for disturbance growth on the wave timescale in the present model involves a time-dependent phase shift along the cycle that is essentially neutral on long timescales. In the more complex models, the phase shift mode presumably still exists and contributes to transient growth, but the additional spatial degrees of freedom allow disturbances that alter the basic synoptic structure in more fundamental ways.

Buizza and Palmer (1995) identify systematic time evolution toward larger spatial scales in growing singular vectors, and infer a nonmodal character of the singular vectors from these changes in their spatial structure. In the present model, the wave scale is fixed, but changes in the relative amplitudes of the wave and mean-flow components can effectively alter the characteristic scale of the disturbance. The Floquet vectors in the present model may thus be seen as a counterexample to this general line of reasoning: they illustrate that modal disturbances to time-dependent basic states can have time-dependent spatial structure. In the case of the Floquet vectors, the spatial structure is time-periodic, but for times shorter than the basic-state period, this periodicity need not be evident. Similarly, Lyapunov vectors, which are the analogs of Floquet vectors for nonperiodic basic states, may in general have nonperiodic spatial structure.

In the present model, the single baroclinic wave is coupled to an infinite set of meridional harmonics of the zonal flow. The model can thus describe zonal-flow disturbances of arbitrarily small meridional scale. As the model also evidently has dissipative, nonperiodic solutions of the general type discussed by Lorenz (1963), it is interesting to examine the character of its ''butterfly effect,'' the influence of small-amplitude, small-scale disturbances on large-scale structure. If the zonal-flow expansion is truncated at a finite $J$, then it is clear that a randomly chosen disturbance will project on the growing Floquet (or Lyapunov) vector, with probability unity. However, the split of the Floquet vectors into wave-dynamical and decaying zonal-flow modes indicates that the projection of small-meridional-scale disturbances on the growing mode will generally be small. If $J$ is large, so that disturbances on the meridional scale of butterflies may be resolved, a randomly chosen disturbance is likely to have extremely small projection on the growing mode. If the timescale required for growth of such an infinitesimal perturbation is longer than the timescale of physical interest, then the small-scale disturbance will have no physical effect on the large-scale flow. This is reminiscent of the classical resolution of the Poincaré recurrence paradox: the timescale of recurrence may exceed the lifetime of the universe.

The insensitivity of the numerical solutions to truncation level $J$ (Fig. 3) suggests that the evolution on the attractor of the higher meridional modes may in principle be parameterized in terms of the wave amplitudes and the lower meridional modes. Independent disturbances of the higher meridional modes would then evidently have to be represented in the truncated system as (stochastic) disturbances of the wave amplitudes and lower meridional modes. Small enough disturbances, however, would still be negligible by the above argument, so that a practical resolution limit would seem to exist beyond which even external disturbances could be safely neglected. The dynamical splitting of the time-dependent disturbance modes that arises in the present mode can evidently increase the spatial scale of this resolution limit, by focusing the projection of the small disturbance on the damped modes, and reducing its pro-

jection on the growing modes. The identification of a similar splitting, and the related spatial scales and structures, in numerical weather prediction models could lead to more efficient initialization techniques.

## 7. Summary

Floquet vectors and singular vectors and the corresponding eigenvalues were computed above for stable and unstable periodic cycles of a simple model of weakly nonlinear baroclinic wave–mean interaction. Each set of vectors was found to divide into two dynamical classes, the first associated with baroclinic wave dynamics and the second with the frictional decay of high meridional modes of the zonal flow. The decompositions of the leading singular vector in terms of the time-dependent Floquet vectors were relatively uniform along the cycle, while the leading singular value depended strongly on initial and optimization times. Disturbance growth in this simple model was found to be related to the wave growth and decay mechanisms associated with the time-dependent basic state.

The results suggest a perhaps surprising connection between the singular vectors (for the chosen norms), which are computed with respect to arbitrary, fixed time intervals along the cycle, and the Floquet vectors, which are defined only as periodic solutions to the disturbance equations linearized about the basic periodic cycles. It is possible that a similar close relation may exist between singular vectors and growing and decaying wave-dynamical modes (where ''modes'' is meant in the sense of Lyapunov vectors for the general, nonperiodic case) in more complex models.

*Acknowledgments.* This research was supported by the Office of Naval Research, Grant N00014-98-1-0813. I am grateful to A. Hindmarsh for assistance with the subroutine LSODAR.

## APPENDIX

### Numerical Methods

The numerical solutions were computed using the public-domain subroutine LSODAR. The root-finding capability of LSODAR was used to construct the Poincaré sections by solving for $B = 0$ and checking $A > 0$. The Floquet problems were solved in the standard way, using LSODAR to integrate the linearized equations and obtain the fundamental matrix, and the matrix eigenvalue solver DGEEV to solve the matrix eigenvalue problem. Unstable periodic cycles were obtained as described above, by spline-fitting the Poincaré map, and using inverse iteration to generate first guesses for a Newton method iteration that in turn used the LU solvers DGETRF and DGETRS. The higher-order cycles were obtained in the standard way, by searching for the sequence of points corresponding to the intersections of the high-order cycle with the ($B = 0$, $A > 0$) Poincaré section, rather than for a single periodic point; this requires increasing the state vector by a factor equal to the order of the cycle, but allows the integration intervals to be limited to single Poincaré return times for each pair of points, preventing convergence failures of the Newton iteration for long-period cycles that would otherwise arise from the finite precision of the initial conditions. It proved necessary to use a successive orthogonalization method to maintain numerical accuracy for the higher-order Floquet problems; that is, by analogy to standard techniques for numerically estimating Lyapunov exponents, the initial conditions for the Floquet calculations were iteratively adjusted according to orthogonalizations of the final states, to allow resolution of the decaying Floquet modes in the final states and thereby improve the conditioning of the associated matrix problem.

## REFERENCES

Artuso, R., E. Aurell, and P. Cvitanović, 1990a: Recycling of strange sets I: Cycle expansions. *Nonlinearity,* **3,** 325–359.

——, ——, and ——, 1990b: Recycling of strange sets II: Applications. *Nonlinearity,* **3,** 361–386.

Buizza, R., 1995: The impact of orographic forcing on barotropic unstable singular vectors. *J. Atmos. Sci.,* **52,** 1457–1472.

——, and T. Palmer, 1995: The singular vector structure of the atmospheric general circulation. *J. Atmos. Sci.,* **52,** 1434–1456.

——, J. Tribbia, F. Molteni, and T. Palmer, 1993: Computation of unstable structures for a numerical weather prediction model. *Tellus,* **45A,** 388–407.

Christiansen, F., P. Cvitanović, and V. Putkaradze, 1997: Spatio-temporal chaos in terms of unstable recurrent patterns. *Nonlinearity,* **10,** 55–70.

Coddington, E., and N. Levinson, 1955: *Theory of Ordinary Differential Equations.* McGraw-Hill, 429 pp.

Cvitanović, P., R. Artuso, R. Mainieri, and G. Vatay, cited 2000: Classical and quantum chaos. Niels Bohr Institute, Copenhagen, Denmark, 682 pp. [Available online at http://www.nbi.dk/ChaosBook/.]

Ehrendorfer, M., and J. Tribbia, 1997: Optimal prediction of forecast error covariances through singular vectors. *J. Atmos. Sci.,* **54,** 286–313.

Epstein, E., 1969: Stochastic dynamic prediction. *Tellus,* **21,** 739–759.

Farrell, B., 1989: Optimal excitation of baroclinic waves. *J. Atmos. Sci.,* **46,** 1193–1206.

——, and P. Ioannou, 1996: Generalized stability theory. Part I: Autonomous operators. *J. Atmos. Sci.,* **53,** 2025–2040.

Joly, A., and A. Thorpe, 1991: The stability of time-dependent flows: An application to fronts in developing baroclinic waves. *J. Atmos. Sci.,* **48,** 163–182.

Klein, P., and J. Pedlosky, 1986: A numerical study of baroclinic instability at large supercriticality. *J. Atmos. Sci.,* **43,** 1243–1262.

Legras, B., and R. Vautard, 1996: A guide to Lyapunov vectors. *Proc. 1995 ECMWF Seminar on Predictability,* Vol. I, Reading, United Kingdom, European Centre for Medium-Range Weather Forecasts, 143–156.

Leith, C., 1974: Theoretical skill of Monte Carlo forecasts. *Mon. Wea. Rev.,* **102,** 409–418.

Lorenz, E., 1963: Deterministic nonperiodic flow. *J. Atmos. Sci.,* **20,** 130–141.

——, 1965: A study of the predictability of a 28-variable atmospheric model. *Tellus,* **17,** 321–333.

Pedlosky, J., 1971: Finite-amplitude baroclinic waves with small dissipation. *J. Atmos. Sci.,* **28,** 587–597.

——, 1987: *Geophysical Fluid Dynamics.* Springer-Verlag, 710 pp.

——, and C. Frenzen, 1980: Chaotic and periodic behavior of finite-amplitude baroclinic waves. *J. Atmos. Sci.,* **37,** 1177–1196.

Phillips, N., 1954: Energy transformations and meridional circulations associated with simple baroclinic waves in a two-level, quasi-geostrophic model. *Tellus,* **6,** 273–286.

Szunyogh, I., E. Kalnay, and Z. Toth, 1997: A comparison of Lyapunov and optimal vectors in a low resolution GCM. *Tellus,* **49A,** 200–227.

Toth, Z., and E. Kalnay, 1997: Ensemble forecasting at NCEP and the breeding method. *Mon. Wea. Rev.,* **125,** 3297–3319.

Trevisan, A., and R. Legnani, 1995: Transient error growth and local predictability: A study in the Lorenz system. *Tellus,* **47A,** 103–117.

——, and F. Pancotti, 1998: Periodic orbits, Lyapunov vectors, and singular vectors in the Lorenz system. *J. Atmos. Sci.,* **55,** 390–398.

Vannitsem, S., and C. Nicolis, 1997: Lyapunov vectors and error growth patterns in a T21L3 quasigeostrophic model. *J. Atmos. Sci.,* **54,** 347–361.